MATERIALS CHEMISTRY FRONTIERS

RESEARCH ARTICLE

View Article Online
View Journal | View Issue

Cite this: *Mater. Chem. Front.*, 2025, **9**, 3548

The interplay between topological defects and CO_2 and NH_3 adsorption in graphene

Daniel Moreno-Rodríguez, *[a] Eva Scholtzová [b] and Hirotomo Nishihara *[cd]

Topological defects in graphene, such as Stone–Wales rearrangements and non-hexagonal ring formations, significantly reshaped its electronic landscape and unlocked new adsorption pathways. Using density functional theory (DFT), this study revealed how these defects influenced the interaction with CO_2 and NH_3 molecules. The findings demonstrated that defect-induced distortions and localized electron density variations created active sites that enhanced molecular interactions. The interplay between defect geometry and molecular orientation governed adsorption strength, with defective graphene models containing 5-, 7- and 8-membered rings, showing enhanced adsorption energies compared to pristine graphene, particularly for NH_3 molecules. Particularly, the model with 5- and 8-membered ring defects (MG8) exhibited the strongest interactions for both CO_2 and NH_3. These results underscore the potential of tailoring graphene's defects for advanced gas storage, sensing, and catalysis applications, opening new avenues for designing more efficient graphene-based materials with tunable adsorption properties.

Received 19th June 2025,
Accepted 16th September 2025

DOI: 10.1039/d5qm00443h

rsc.li/frontiers-materials

Introduction

Graphene is a two-dimensional (2D) material formed by a one-atom-thick planar sheet of arranged sp^2 hybridised carbon atoms packed in a honeycomb-like lattice.[1] The properties derived from the structure and composition of graphene[2–6] make it a material with a wide range of possible applications,[7] *e.g.*, energy storage,[8,9] supercapacitors,[10–12] sensors,[13–15] photodetectors,[16–18] composite materials,[19–21] membranes,[22] drug delivery and biomedical engineering.[23–26] The synthesis of 2D materials like graphene inevitably generates defects, *e.g.*, grain boundaries between neighbouring grains with a misorientation[27] and point defects, such as vacancies, dislocations and functionalised groups.[28] These defects impact the topology and destroy the geometric symmetry in the structure (distort the pristine lattice), affecting the physicochemical, thermal, mechanical, magnetic, and electrical properties of 2D materials.[29–32] Different types of defects induce distinct changes in electronic and mechanical properties, while the density of defects determines the overall impact. Additionally, the specific configuration and clustering of defect sites affect local strain distribution and structural integrity. For instance, the density and distribution of vacancy defects can affect the elastic and Young's moduli of graphene,[33,34] and defects can increase the active sites on the graphene surface.[35]

Some intrinsic defects, like adjacent pairs of heptagonal and pentagonal rings, may appear by rotating a single pair of carbon atoms 90°. This point defect is known as the Stone–Wales (SW) defect, with a formation energy of approximately 5 eV.[30,36,37] Besides, the C atom vacancies in graphene can favour the migration of the adjacent atoms, forming five-membered, eight-membered or/and nine-membered rings,[38–41] *e.g.*, single vacancies can lead to the formation of five- and nine-membered rings,[42] whereas the divacancy can further transform into five- and eight-membered rings or five- and seven-membered rings.[39,43] Furthermore, the double vacancy in graphene is more stable and less movable, with a migration barrier of approximately 7 eV, than the single one, with a migration barrier of 1.3 eV.[44] In addition, five- and seven-membered rings can be generated through dislocations and grain boundaries.[45,46] Moreover, bonds can be affected by the defects compared to pristine graphene, *e.g.*, with a single vacancy defect exhibiting sp^2 bonding, whereas the SW defects show nearly sp bonding. The current–voltage decrease and the transmission probability are affected by the presence of defects, particularly with the vacancy defects causing a larger voltage reduction. Additionally, the SW defects could

[a] *Department of Mechanical and Aerospace Engineering, Sapienza University of Rome, Via Eudossiana 18, 00184 Rome, Italy. E-mail: daniel.morenorodriguez@uniroma1.it*
[b] *Institute of Inorganic Chemistry, Slovak Academy of Science, Dúbravská cesta 9, 84536 Bratislava, Slovakia*
[c] *Institute of Multidisciplinary Research for Advanced Materials, Tohoku University, 2-1-1, Katahira, Aoba-ku, Sendai, 980-8577, Japan. E-mail: hirotomo.nishihara.b1@tohoku.ac.jp*
[d] *Advanced Institute for Materials Research (WPI-AIMR), Tohoku University, 2-1-1, Katahira, Aoba-ku, Sendai, 980-8577, Japan*

potentially open an electronic energy band gap in graphene, enhancing its suitability for transistor applications.[37]

Various 2D carbon materials, such as penta-graphene (consisting of pentagonal rings), pha-graphene (with hexagonal and pentagonal rings), Ψ-graphene (composed of heptagonal and hexagonal rings), and popgraphene (PopG) featuring interconnected pentagonal and octagonal rings, exhibit unique structures and properties, with potential applications spanning electronics, spintronics, catalysis, and energy storage, *e.g.*, PopG presented physisorption in pristine and vacancy structures and chemisorption in doped variants for O_2 molecules.[47]

The defect sites may enhance or diminish graphene's ability to adsorb or catalyse chemical reactions, impacting its potential applications in sensors, catalysis, and surface modification. For instance, oxygen molecules dissociate into active oxygen atoms on both the edge and basal plane of graphite, with single active oxygen atoms exhibiting higher reactivity and readily adsorbing onto defect sites, such as SW defects and single vacancy sites, on the graphene surface, leading to exothermic chemisorption reactions and enhanced oxidized reactivity, suggesting catalytic effects in graphene oxidation.[48] Besides, some strategies were explored to induce band gaps in graphene, *e.g.*, by surface functionalization and doping to modify its electronic properties, bringing some potential applications in sensors and pollutant detection due to its high sensitivity and conductivity. For example, vacancy-defected graphene doped with B, N, and S atoms exhibited distinct electronic properties (*e.g.*, band gap), influencing the adsorption of formaldehyde (H_2CO) molecules, suggesting potential for sensitivity in graphene-based gas sensors.[49] Furthermore, strain-induced variations in graphene layers affect reactivity and adsorption behavior. Under tensile strain, graphene's electronic structure is altered as sp^2 hybridized bonds weaken, forming localized dangling bond states that enhance chemical reactivity, while compressive strain reduces reactive sites by delocalizing electron wavefunctions, rendering the graphene surface less chemically active.[50]

However, the most common synthetic strategies present significant limitations. For instance, nitrogen doping only moderately enhances CO_2 physisorption (-0.2 to -0.4 eV) compared to pristine graphene, primarily through increased basicity,[51] while its effect on NH_3 adsorption remains weak and highly dependent on dopant concentration.[52] Conversely, vacancy defects provide unsaturated carbon sites that enable much stronger, often chemisorptive, binding with energies for CO_2 approaching -1.0 eV,[53] but these sites are inherently unstable due to dangling bonds, which can lead to structural degradation or passivation. In this context, topological defects offer a distinct and potentially superior pathway. Unlike doping or vacancies, their enhanced reactivity arises from stable topological rearrangements of the carbon network, such as non-hexagonal rings, which generate intrinsic, highly localized electronic states without the need for foreign atoms or unstable, unsaturated sites.

Non-hexagonal defects, including SW defects, are often referred to as topological defects and are particularly prominent in three-dimensional (3D) structures with curved graphene architectures. In particular, a 3D graphene material known as graphene mesosponge (GMS),[54] which contains a large number of topological defects without graphene edge sites, has been experimentally confirmed to exhibit topological defects, including SW defects, through direct observation and Raman spectroscopy.[55] It has been demonstrated that these topological defects serve as anchoring sites for catalysts[56,57] and exhibit favorable catalytic activity as cathode materials in Li–O_2 batteries[55] without compromising oxidation resistance,[58] unlike graphene edge sites. Therefore, a deeper understanding of the properties and functionalities of topological defects is crucial for further developing 3D graphene materials.

The primary objective of this work is to investigate how various defects in graphene, such as SW defects (5- and 7-membered rings), found in GMS,[54,55] as well as defects with 5- and 8-membered ring moieties affect the electronic structure and properties of materials like GMS. Specifically, the present study focused on the interactions and adsorption behavior of small molecular species like CO_2 and NH_3 molecules.

Methodology

Computational details

The optimization of the models was performed using density functional theory (DFT) as implemented in the Vienna ab initio Simulation Package (VASP).[59,60] The exchange–correlation energy was described using generalized gradient approximation (GGA) with the Perdew–Burke–Ernzerhof (PBE) functional.[61] The van der Waals interactions present in the studied systems were accounted for using the DFT-D3 scheme for dispersion corrections.[62]

For geometry optimizations and electronic structure calculations, a Monkhorst–Pack grid with a density of $11 \times 11 \times 1$ *k*-points per reciprocal unit cell was used. Convergence criteria were set to 10^{-6} eV for energy and 0.01 eV Å^{-1} for force.

For band structure calculations, a denser *k*-point path along the high-symmetry points Γ–M–K–Γ was employed. Density of states (DOS) calculations utilized a Monkhorst–Pack grid with a density of $21 \times 21 \times 1$ *k*-points, and the tetrahedron method with Blöchl corrections was used to obtain appropriate DOS values.

Model preparation

Three models were prepared: the pristine graphene (G) structure, the modified graphene structures with the SW defect (MG7) and the defect forming pentagonal and octagonal rings (MG8). The proposed final G and MG7 models contained 64 carbon atoms each, while the MG8 model consisted of 52 carbon atoms. In the defective models, a substantial proportion of carbon atoms formed defects ($\sim$56% for MG7 and $\sim$54% for MG8). For adsorption studies, three different initial positions of the CO_2 and NH_3 molecules were chosen for each model to explore possible interacting arrangements, *e.g.*, for NH_3, the configurations tested were: (1) the N-lone pair oriented toward the surface, (2) H atoms oriented toward the surface, and (3) a tilted configuration. These configurations,

selected from a broader exploration (Fig. S1 and S2), were sufficient to identify the key adsorption interactions and low-energy states, with optimized positions consistently converging to similar arrangements.

Electronic structure analysis

The density-derived electrostatic and chemical (DDEC6) method[63,64] was employed to calculate partial charges (δ) and bond orders (BO). The topology of the electron density (ρ), particularly bonding characteristics, was studied using the electron localization function (ELF)[65] and Laplacian electron density ($\nabla^2\rho(r_b)$).[66]

Adsorption analysis

The electron density difference (EDD) was calculated for the optimized graphene structures with adsorbed CO_2 and NH_3 molecules to investigate electron density distribution among atoms and the formed interaction types. The adsorption energy (AE) of CO_2 and NH_3 molecules was calculated using the equation $AE = E_{product} - (E_{carbon\ sheet} + E_{molecule})$, where $E_{product}$ is the total energy of the adsorbed system, $E_{carbon\ sheet}$ is the energy of the isolated graphene sheet, and $E_{molecule}$ is the energy of the isolated adsorbed molecule. During calculations, the adsorbed molecule could relax and explore stable positions on the graphene surface through geometry optimization, ensuring the system reached the lowest-energy configuration and provided reliable adsorption energies and stable molecular arrangements.

Results and discussion

Structure and electron density topology of graphene and defects

After the energy minimisation, the C atoms presented different bond lengths, BO and δ, according to their neighbours' positions, *i.e.* 5-, 6-, 7- or 8-membered rings (Fig. S3). The defect formation energies for MG7 and MG8 are shown in Table S1.

The optimised structure of the G model (Fig. 1a) showed the expected and homogeneous bond length of about 1.42 and 1.43 Å, which was in agreement with the calculated BO (Fig. S3). In the optimised MG7 model (Fig. 1b), with 5–7 membered rings, the bond lengths exhibited a wider range (from 1.55 to 1.40 Å, with an average ± standard deviation value of 1.43 ± 0.03 Å), following a similar trend to their BO, *i.e.* the shorter the bond length, the stronger the bond (Fig. S3), showing the longest (weakest) C–C bonds among the three models. Furthermore, MG8 (Fig. 1c), with 5–8 membered rings, exhibited weaker bonds than G but stronger bonds than the MG7 model, having bond lengths ranging from 1.47 to 1.39 Å, with an average ± standard deviation value of 1.43 ± 0.02 Å (Fig. S3). However, in the MG8 model, there was no complete correlation between the bond length and the BO as observed in the other models: some bonds presented a higher ρ with a longer bond length than expected.

According to the topology of ρ, δ has shown a homogeneous distribution of ρ in the G structure (Fig. S4a). Otherwise, the MG7 model presented a higher accumulation of ρ (lower δ^-) in the frontier between the SW defect, 5-,7-membered rings, and the regular 6-membered rings. In contrast, there was a depletion of ρ (higher δ^+) on the 5- and 7-membered rings (Fig. S4b). In the 8- and 5-membered rings in the MG8 model, there was a spot with the highest ρ concentration (lowest $\delta^- = -0.55\ e$), with a depletion of ρ in the rest of the defects compared to the neighbouring 6-membered rings (Fig. S4c). This agrees with the BO, where the bond strength is related to the ρ shared by the C atoms (Fig. 1), as shown by the ELF topology of the different models (Fig. S5).

The $\nabla^2\rho(r_b)$ analysis has shown that, as expected, the more the localisation of ρ among the C atoms, the stronger the bond. For instance, ρ was evenly localised between the bonded C atoms (Fig. S5a and d). Otherwise, comparing the delocalised electron density, the 5- and 6-membered rings presented a more significant ρ delocalisation than the 7- and 8-membered rings (Fig. S5b, c and e, f), as reflected in the difference in bonding strength.

In more detail, the C–C bonds displayed similar ρ topologies in the G model, where the strongest bond had a BO of 1.22 *e*

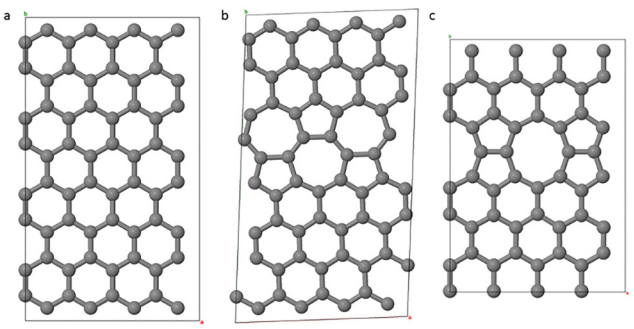

Fig. 1 Optimised structures of G (a), MG7 (b) and MG8 (c) models, shown in the c-view.

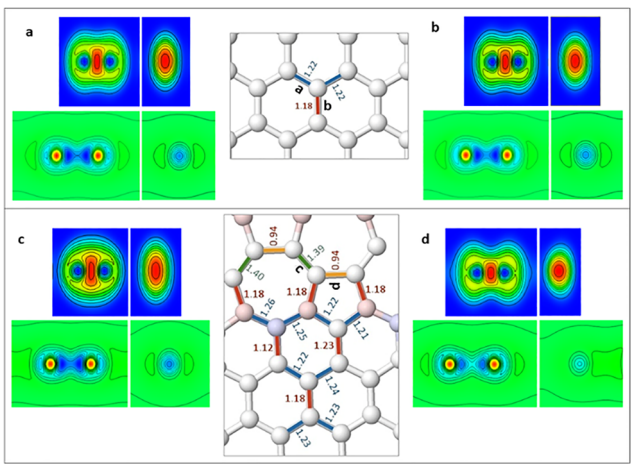

Fig. 2 Different bonds in the G (a) and (b) and MG7 (c) and (d) models according to their BO, coded by colors (red, blue, green and yellow). The ELF (up) and $\nabla^2\rho(r_b)$ (down), along (left) and across (right) sections.

and the weaker 1.18 *e*, corresponding to 1.42 (Fig. 2a) and 1.43 Å bond lengths (Fig. 2b), respectively.

The strongest bond found in the MG7 model had a bond length of 1.40 Å with a BO of 1.39 *e* (Fig. 2c), presenting a highly localised ρ in the bonding area besides the delocalised ρ towards the 5- and 7-membered rings. However, the weakest and longest bond (1.55 Å) in the structure had a thinner localised ρ area, with a BO of 0.94 *e* (Fig. 2d), and the delocalised ρ appeared in the inner part of the 5-membered ring next to the bond.

The strongest C–C bond found in the MG8 model had a BO value of 2.50 *e* and a bond length of 1.39 Å (Fig. 3a), which presented delocalised ρ towards one of the 5-membered rings next to it. The weakest bond with a BO value of 2.04 *e* and a bond length of 1.47 Å (Fig. 3b) was located in a 6-membered ring next to an 8-membered ring, showing that the delocalised ρ was less pronounced in this ring than in the 5-, 6- and 7-membered rings. This is also observed in a stronger bond, with a BO value of 2.48 *e* and a bond length of 1.43 Å in a 5-membered ring and between two 8-membered rings, where the bond did not show delocalised ρ along the 8-membered ring (Fig. 3c).

However, next to the C atom with the highest ρ, there was a bond with the highest BO in the MG8 structure, although the length did not correspond: BO of 2.54 *e* and bond length 1.45 Å (Fig. 3d). This asymmetry of the bond's ρ could be caused by the C atom with the highest charge that "pushes away" the C atom bonded to it, generating this longer bond but still with a larger ρ on average between both atoms.

Besides, the ELF and Laplacian methods showed that the ρ was delocalised to the 5-membered rings (Fig. 3d), while also showing an asymmetry towards the C atom with the highest δ^- (-0.55 *e*) in the defect. This difference between a higher δ^- and the surroundings with a lower ρ can facilitate interactions, *e.g.*, with other molecules.

As shown above, the presence of 5-, 7-, and 8-membered rings introduced localized distortions in graphene and, consequently, its topology. These defects can significantly affect the bonding environment of neighboring carbon atoms.

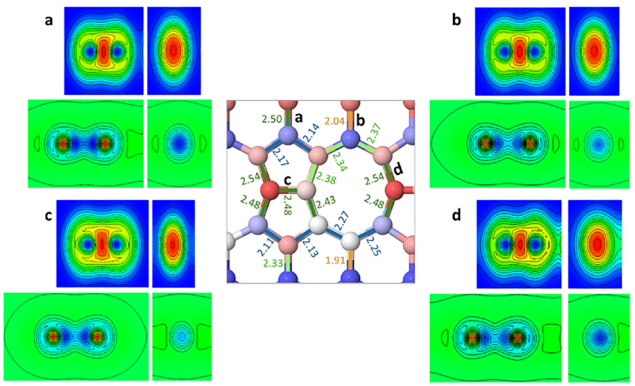

Fig. 3 Different bonds in the MG8 model according to their BO, coded by colours (blue, green, light green and orange). The ELF (up) and $\nabla^2\rho(r_b)$ (down), along (left) and across (right) sections.

Analyzing the sum bond order (SBO) values can provide insights into the local bonding properties and the structure of graphene sheets. For the G model, the SBO values for all C atoms were very homogeneous (SBO = 3.99 *e*) due to the delocalised π-electrons contributing to the uniformity of bonding interactions and bond orders across the lattice. On the other hand, in the MG7 and MG8 models, the presence of defects disrupts the regular hexagonal lattice structure, leading to alterations in bond lengths and bond angles and, consequently, in their ρ topology. For instance, in the MG7 model, the 6-membered rings presented an average SBO of 4.00 *e*, where the variations in SBO corresponded to those C atoms in the vicinity of the defect, which were also a part of the defect. In the same way, for the C atoms that formed the 5- and 7-membered rings, the average SBOs were 3.95 *e* and 3.89 *e*, respectively. In the MG7 model, the delocalized ρ was predominantly observed within the 6-membered rings, followed by the 5-membered rings, with a lower presence in the 7-membered rings. These observations were consistent with the findings of the ELF and Laplacian electron density analysis (Fig. S5b and e).

In the case of the MG8 model, the delocalised ρ found in the 6-membered rings displayed an average SBO value of 3.80 *e*, whereas for 5- and 8-membered rings the values were 4.01 *e* and 3.91 *e*, respectively. The relative difference in the ρ value of the 6-membered ring with respect to the MG7 model was caused by the participation of those 6-membered rings (2/3 of the total rings) in the 5- and 8-membered rings as well.

Moreover, the higher ρ in the defects was primarily due to specific carbon atoms with high δ rather than delocalized ρ on the rings, although 5-membered rings seemed to exhibit more delocalized ρ than 8-membered rings (Fig. S5c and f).

The disruption of conjugation in the graphene structure, *i.e.* the highly delocalized π-electron systems, was due to the 5-, 7- and 8-membered ring defects. It was shown that if part of the six-membered rings shared atoms with these defects, it further disrupts the conjugation pathway, leading to more localised ρ, *e.g.*, the higher δ^- found at the proximity of the defects in MG7 (Fig. S4b).

Adsorption of CO_2 and NH_3

Defects in the graphene lattice can create active sites for adsorption, potentially enhancing its adsorption capacity. To investigate this, the interactions of CO_2 and NH_3 with G, MG7, and MG8 structures were studied, emphasizing the role of 5-, 7-, and 8-membered ring defects in determining graphene's behaviour.

The orientation of defects critically governed adsorption configurations. In MG7, CO_2 aligned parallel to the surface (Fig. 4c), maximizing van der Waals interactions, while NH_3 tilted to optimize lone-pair donation to electron-rich defect sites (Fig. 4d). For MG8, asymmetric charge distribution further localized NH_3 near the defect periphery (Fig. 4d), enhancing adsorption. For CO_2 adsorption, the optimized models revealed that the molecules preferentially adopted a parallel arrangement relative to the graphene surface in most configurations,

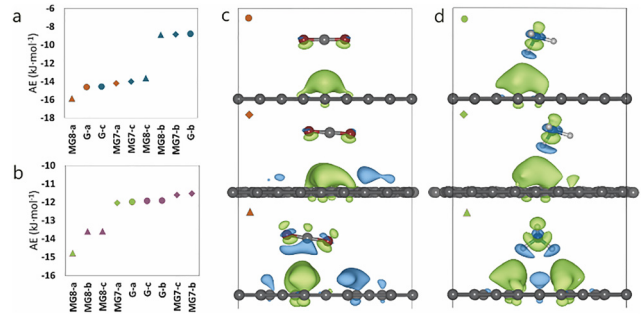

Fig. 4 Adsorption energies (AE) for CO_2 (a) and NH_3 (b) on pristine graphene (G) and defected graphene surfaces (MG7 and MG8). Different adsorption configurations are denoted by -a, -b, and -c. The electron density difference (EDD) isosurfaces for CO_2 (c) and NH_3 (d) adsorbed on G, MG7 and MG8 (from top to bottom). Green and blue isosurfaces represent electron accumulation and depletion, respectively. The isosurface value was set to ± 0.002 e Å^{-3}.

resulting in the lowest adsorption energies (AE; Fig. 4a and b) and thus more stable configurations (Fig. S6).

MG8 obtained the lowest AE (-15.85 kJ mol^{-1}), followed by pristine graphene (-14.60 kJ mol^{-1}) and MG7 (-14.19 kJ mol^{-1}). In pristine graphene, CO_2 molecules exhibited a preferred parallel orientation, maximizing van der Waals interactions with the surface. The molecules tended to centre over regions of favourable charge distribution, typically the centres of 6-membered rings (Fig. S6). However, in the presence of defects (MG7 and MG8), the CO_2 molecules displayed a slight tilt and displacement towards higher electron density (Fig. 4c), likely facilitating stronger, albeit still predominantly van der Waals, interactions.

In contrast to CO_2, NH_3 molecules exhibited a preferential tilting towards the graphene surface, optimizing interactions between their lone electron pairs and the surface. This orientation was particularly evident at defect sites (Fig. S7 and S8). The adsorption energies for NH_3 reflected this trend, showing a clear increase in interaction strength with increasing defect complexity: MG8 exhibited the strongest interaction (-14.78 kJ mol^{-1}), followed by MG (-12.05 kJ mol^{-1}) and pristine graphene (-11.99 kJ mol^{-1}).

This difference in adsorption energies suggests that topological defects create more favourable binding sites for NH_3 molecules, likely due to a combination of factors including: (1) the accumulation of electron density (as evidenced by the EDD maps in Fig. 4d) around the defect sites, leading to stronger electrostatic interactions; and (2) enhanced dipole moments induced by the defects interacting with NH_3 (Fig. 4d).

A comprehensive DDEC6 charge analysis (Table S2) was performed to elucidate the adsorption mechanisms. For CO_2, the negligible charge transfer (<0.01 e) across all models confirms a physisorption process dominated by van der Waals forces. This was visually supported by the EDD maps (Fig. 4c), which show only minimal and diffuse regions of electron redistribution.

For NH_3, while the net charge transfer was also small (~ 0.007 e), the local charge environment was crucial. The MG8 defect generated highly electron-rich carbon sites (δ^- up to -0.07 e), which engaged in strong electrostatic interactions with the positively charged NH_3 hydrogens ($\delta^+ = 0.29$ e), as evidenced by an attractive charge product of -0.018 e^2. The EDD maps provided a clear visual confirmation of this charge polarization: pronounced electron accumulation (green) is localized on these specific carbon atoms at the defect site, while distinct electron depletion (blue) is observed around the hydrogen atoms of the NH_3 molecule (Fig. 4d).

This combination of quantitative charge analysis and visual EDD evidence robustly confirmed that the greater adsorption of NH_3 on MG8 is primarily driven by localized electrostatics, a direct consequence of the topological defect's electronic structure.

Thus, disrupting the π–π interactions on defect sites allowed for localized charge accumulation/depletion, facilitating and enhancing the interaction with NH_3, as shown in Fig. S8 and Fig. 4c and d.

Analysis of molecular distances revealed distinct interaction patterns for both CO_2 and NH_3 with the graphene surfaces. For CO_2 adsorption, distances between the molecule and the nearest C atom of the graphene surface ranged from 3.29 Å to 3.56 Å. In parallel configurations, distances typically ranged from 3.39 to 3.47 Å, suggesting a more distributed van der Waals interaction. For perpendicular configurations, CO_2 molecules were centered over 6-, 7-, and 8-membered rings (Fig. S6), exhibiting distances ranging from 3.40 to 3.42 Å. This orientation likely resulted from interactions between one of the oxygen atoms of CO_2 and regions of electron depletion on the graphene surface, particularly around the centres of these rings (Fig. S8). For NH_3 adsorption, the H$\cdots\pi$ distances were generally shorter (2.73 to 3.15 Å), indicating stronger localized interactions. The shortest distance (2.74 Å) was observed in configuration G-a and MG7-a, where one H atom of NH_3 was tilted towards the graphene surface, forming weak interactions with the π-electron systems (Fig. 4d). Similarly, the NH_3 interaction in MG8-a was stronger than those in G and MG7 (Fig. 4b), with the graphene surface at distances of 2.76 and 2.96 Å. The generally shorter distances observed for NH_3 compared to CO_2 suggest stronger localized interactions, particularly when the molecule adopted tilted configurations that allow for stronger interactions with the surface.

Systematic analysis of NH_3 adsorption across graphene variants revealed a progressive enhancement from pristine to defective structures. Pristine graphene (G) exhibited two weak interactions (NH$\cdots\pi$: 2.74 Å, BO = 0.02; 2.85 Å, BO = 0.01). Similarly, the MG7 structure manifested two weak interactions (NH$\cdots\pi$: 2.74 Å, BO = 0.02; 2.84 Å, BO = 0.02) with a slight increase in its interactions. A defective MG8 configuration developed multiple interacting sites, presenting four weak interactions (NH$\cdots$C: 2.77 Å, BO = 0.02; 2.80 Å, BO = 0.02; 2.97 Å, BO = 0.01; 2.97 Å, BO = 0.01). Despite nearly identical net charge transfer per NH_3 molecule (~ 0.007 e) in all models, the MG8 system exhibited 23% stronger adsorption (-14.78 kJ mol^{-1} *vs.* -11.99 kJ mol^{-1} in pristine graphene) through electrostatic enhancement at defect sites (Fig. S4). Thus, the localized charge polarization at defect sites

(*e.g.*, C δ^- = −0.07 *e* in MG8 *vs.* C δ^- = −0.005 in G) enabled the formation of NH_3 interactions with stronger electrostatic character compared to pristine graphene, which had a major dispersion interaction component (Table S2).

CO_2 adsorption was enhanced in defective graphene through geometric optimization rather than electronic effects. The 5–8-membered rings in MG8 reduced the closest CO_2–graphene contact distance from 3.44 Å (pristine graphene) to 3.29 Å while enabling interaction sites (*e.g.*, 3.29 Å, BO = 0.02 or 3.46 Å, BO = 0.01). These structural adjustments strengthened van der Waals forces through closer proximity (enhancing the $1/r^6$ dependence of dispersion interactions) and cooperative multi-site engagement, yielding an 8.6% adsorption energy increase (−14.60 to −15.85 kJ mol^{-1}). Unlike NH_3's charge-assisted binding, CO_2's physisorption relied entirely on defect-enabled geometric advantages, optimal topology for molecular accommodation and simultaneous contact points, without significant charge transfer (< 0.01 *e*).

Furthermore, MG7 and MG8 defects remained stable with only minor distortions, showing that adsorption preserves the non-hexagonal rings (Fig. S6 and S7). Evaluating cycling stability through desorption barriers and finite-temperature effects is left for future work, as it is beyond the scope of the present study.

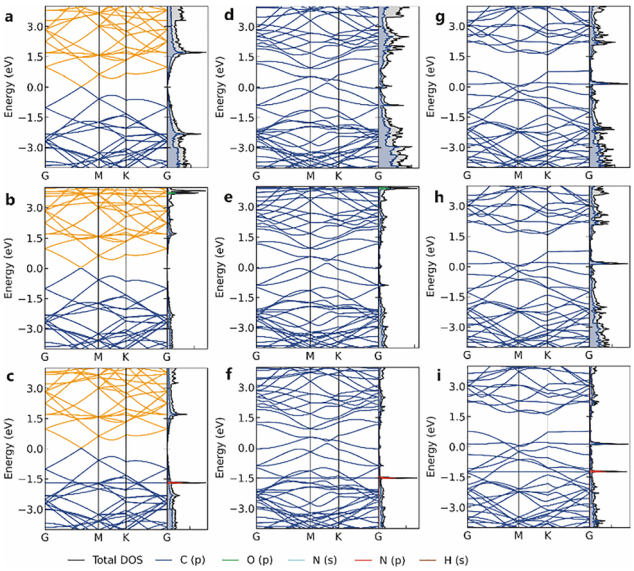

Fig. 5 Band structure and DOS for pristine and defected graphene with molecular adsorption: G (a), CO_2-G (b), NH_3-G (c), MG7 (d), CO_2-MG7 (e), NH_3-MG7 (f), MG8 (g), CO_2-MG8 (h), and NH_3-MG8 (i). The band structures were plotted along the high-symmetry path Γ–M–K–Γ. The DOS plots showed the total DOS (black) and orbital-projected contributions (PDOS) from C(p) (blue), O(p) (green), N(s) (cyan), N(p) (red), and H(s) (brown). The Fermi level was set to 0 eV.

Electronic structures of pristine and defective graphene

The band structure analysis demonstrated significant changes in graphene's electronic properties caused by topological defects (Fig. 5). Pristine graphene (G) exhibits a small direct bandgap of 0.057 eV, with the valence band maximum (VBM) and conduction band minimum (CBM) positioned at the same *k*-point in the Brillouin zone. This small but non-zero bandgap arises due to finite-size effects in the computational model, deviating slightly from graphene's ideal zero-gap semimetallic nature.

Topological defects significantly alter graphene's electronic properties. Both MG7 and MG8 models exhibit negative bandgaps (−0.252 eV and −0.074 eV, respectively), indicating a transition to metallic behaviour. The Fermi energy drops from −2.861 eV in G to −3.084 eV in MG7 and −3.174 eV in MG8, reflecting the formation of defect-induced states that disrupt the π-electron network. This behaviour mimics a p-type doping effect, where defects act as acceptor states, enhancing electronic conductivity.

Impact of molecular adsorption

Molecular adsorption induces noticeable changes in the electronic structure of graphene models. For G, molecular adsorption only slightly affected the bandgap and Fermi energy. G-CO_2 retained a direct bandgap of 0.056 eV, similar to pristine G, with a slight upward shift in Fermi energy to −2.838 eV. In contrast, G-NH_3 displayed a comparable bandgap (0.056 eV) but showed a more pronounced downward shift in Fermi energy to −2.953 eV, indicating charge transfer between NH_3 and the graphene surface.

Defective graphene exhibited a more significant response to adsorption. MG7-CO_2 showed a marginal increase in the negative bandgap (−0.253 eV from −0.252 eV), while MG7-NH_3 exhibited a further increase to −0.261 eV. These changes were accompanied by Fermi energy shifts to −3.026 eV for MG7-CO_2 and −3.146 eV for MG7-NH_3. Similarly, MG8-CO_2 displayed a slight increase in negative bandgap (−0.073 eV from −0.074 eV), while MG8-NH_3 showed a reduction to −0.063 eV. The corresponding Fermi energy shifts to −3.251 eV for MG8-CO_2 and −3.370 eV for MG8-NH_3 were consistent with electronic changes caused by the defect. Additionally, a more detailed band structure analysis revealed significant changes across the different graphene systems, with subtle modifications upon molecular adsorption. Pristine graphene (Fig. 5a) exhibited characteristic linear Dirac bands meeting at the K point near the Fermi level (*E* = 0 eV), indicating enhanced charge transfer, particularly during NH_3 adsorption (Fig. S9). The defective structures MG7 (Fig. 5d) and MG8 (Fig. 5g) showed notable modifications compared to pristine graphene.

MG7 displayed increased band crossings at the Fermi level, particularly along the M–K path, indicating a transition towards more metallic behaviour. MG8 exhibited the most pronounced changes among the structures, showing multiple bands crossing the Fermi level along the entire Γ–M–K–Γ path and a more complex band structure, especially in the range of −2 eV to 2 eV.

The adsorption of CO_2 on G (Fig. 5b), MG7 (Fig. 5e), and MG8 (Fig. 5h) surfaces induced minor perturbations in the electronic structure of each respective model, largely maintaining their overall band features. The changes were subtle and primarily manifested as slight modifications in band curvature

and dispersion. However, the most notable change across all models was observed with NH_3 adsorption (Fig. 5c, f and i), where a distinctive feature appeared in the form of a relatively flat band just below the Fermi level, around −0.5 eV. This band corresponds to the sharp peak in the N(p) DOS, indicating the introduction of localized N-derived states.

The progression from pristine to defective structures demonstrated a systematic increase in the density of states near the Fermi level. This trend, combined with the consistent appearance of the N(p) derived band upon NH_3 adsorption, suggests a potential increase in the chemical reactivity of the structures, particularly towards NH_3 molecules.

Defect-enhanced interactions

Defects significantly amplified graphene's molecular adsorption capabilities, especially for NH_3. Across all models, NH_3 adsorption caused a consistent downward shift in Fermi energy (*e.g.*, G: −2.953 eV, MG7: −3.146 eV, and MG8: −3.370 eV), attributed to an increase in ρ between NH_3 and the graphene surface.

This interaction was predominantly driven by hydrogen bonding, with NH_3 molecules acting as hydrogen bond donors to the π-electron network.

It is important to note the distinction between classical hydrogen bonding and interactions with graphene: while classical hydrogen bonds involve X–H donors and lone pairs on electronegative atoms, and X–H$\cdots\pi$ interactions with pristine graphene are typically weak due to delocalized electrons, topological defects such as non-hexagonal rings localize charge and enable stronger, more directional interactions resembling partial charge-assisted hydrogen bonds.

The defective models MG7 and MG8 exhibited more pronounced Fermi energy shifts, suggesting that defects created favourable localized sites for interacting through alterations in the electronic density. This agreed with the finding in the ρ topology (Fig. S4) and EDD maps for MG7 and MG8 models (Fig. 4c and d). CO_2 interactions, by contrast, were weaker and primarily mediated by van der Waals forces. In pristine graphene, CO_2 adsorption resulted in a slight upward shift in Fermi energy (−2.838 eV), indicative of weak physisorption. In defective models, minor downward shifts in Fermi energy (*e.g.*, MG7-CO_2: −3.026 eV and MG8-CO_2: −3.251 eV) suggested enhanced van der Waals interactions at defect sites, likely due to localized changes in the electronic structure.

Electronic structure analysis *via* density of states

The DOS provided crucial insights into the electronic structure of the graphene models. Pristine graphene exhibited a characteristic V-shaped DOS profile (symmetrically at approximately −2.34 eV and 1.70 eV) near the Fermi level (set at 0 eV), a signature of its semimetallic nature (Fig. 5a and Fig. S8). This sharp peak arose from the linear dispersion of π and π* bands at the K point, resulting in a low density of states at the Fermi level. The projected DOS revealed that carbon p-orbitals dominate the electronic states near the Fermi level, consistent with the sp^2 hybridization in graphene. Other peaks appeared at higher energies (±4–6 eV) due to σ bonds (Fig. S10).

The introduction of defects significantly altered the electronic surface. Unlike pristine graphene's characteristic V-shaped profile, MG7 exhibits multiple peaks near the Fermi level and a more irregular DOS distribution (Fig. 5d and Fig. S10). Besides, a noticeable increase in the DOS was observed at the Fermi level, indicating the emergence of localized states. This increase in states at the Fermi level suggested enhanced metallic character, which agrees with the band structure analysis. Moreover, several peaks appeared below 0 eV (*i.e.* valence band), around −5.5 eV, −4.5 eV, and a broader feature between −3 and −2 eV (Fig. 5d). Some peaks were also observed above 0 eV (*i.e.* conduction band), approximately at 2 eV, 3 eV, and a sharp peak at 6 eV (Fig. S10). There was also a small but noticeable peak near 0 eV (Fig. 5d and Fig. S10). The overall DOS showed less intense features compared to MG8 but still deviates from pristine graphene's V-shaped profile over the energy range from −4 eV to 4 eV (Fig. 5d and Fig. S10). The C(p) orbital contribution remained dominant, together with the asymmetric distribution of states and the presence of additional peaks around the Fermi level, suggesting that the defect-induced states primarily arise from localized p-orbital perturbations.

The MG8 model exhibited the most dramatic modification of the electronic structure. A sharp and intense peak emerged at the Fermi level (Fig. 5g and Fig. S10), signifying a high DOS and metallic character. This distinct feature, absent in pristine graphene and less prominent in MG7, highlighted the significant impact of the eight- and five-membered ring defects in the graphene electronic structure. The overall DOS profile of MG8 was characterized by increased irregularity, reflecting the substantial structural distortion introduced by the defects. The C(p) projected DOS closely followed the total DOS pattern, confirming that these defect-induced states primarily originate from carbon p-orbitals.

To assess the impact of defects and adsorbates on the electronic transport properties, the Fermi integral was calculated to quantify the number of available electronic states near the Fermi level (Table S3), *e.g.*, the DOS available for charge transfer. Thus, the Fermi integral increased substantially from pristine graphene (0.436) to defective models (MG7: 1.629, MG8: 2.847), with further increases upon NH_3 adsorption (NH_3-MG8: 3.755). This trend correlated with the transition towards metallic behaviour observed in band structure analysis. The centre of mass of the DOS shifted to lower energies in defective models, particularly for MG8 (−0.777 eV), suggesting the introduction of new electronic states below the original Fermi level. Notably, the percentage of DOS within 1 eV of the Fermi level increased in defective models, with NH_3-MG8 exhibiting the highest value (3%), indicating enhanced reactivity. The p-orbital contributions remained consistently high (around 70–71%) across all models, reflecting the preservation of graphene's sp^2 hybridization despite defects and adsorption.

To gain further insights into the electronic structure modifications induced by defects and adsorbates, the projected density of states (PDOS) of the systems were analysed (Fig. 6).

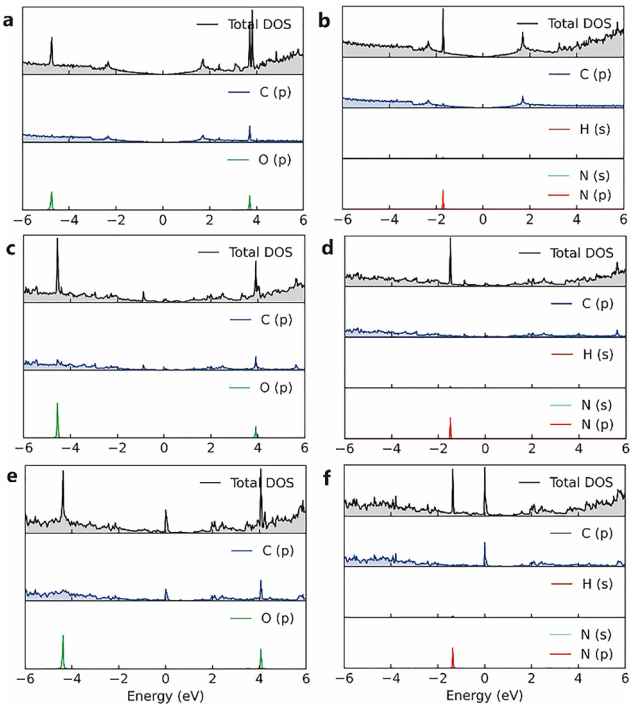

Fig. 6 Orbital-projected density of states (PDOS) for CO_2 and NH_3 adsorption. PDOS for CO_2 adsorption on G (a), MG7 (c), and MG8 (e), showing total DOS (black), C(p) (blue), and O(p) (green) contributions. PDOS for NH_3 adsorption on G (b), MG7 (d), and MG8 (f), showing total DOS (black), C(p) (blue), H(s) (brown), N(s) (cyan), and N(p) (red) contributions. The energy is referenced to the Fermi level (0 eV).

For CO_2 adsorption, C(p) states dominated the overall DOS profile, particularly near the Fermi level, while O(p) states showed sharp, localized peaks around −5 eV and 4 eV, suggesting minimal hybridization with graphene. Similarly, for NH_3 adsorption, N(p) states exhibited a characteristic sharp peak around −2 eV, while H(s) contributions were minimal. Both CO_2 and NH_3 adsorption showed similar trends across the graphene models: defective structures (MG7 and MG8) displayed increased DOS near the Fermi level compared to pristine graphene (G), indicating enhanced reactivity. This was particularly evident in MG8, which exhibited the highest density of states at the Fermi level, consistent with its more pronounced metallic character compared to the other models.

Defective structures also exhibited broader DOS distributions, suggesting increased electronic state availability. The total DOS near the Fermi level increased in the order G < MG7 < MG8 for both adsorbates, implying enhanced chemical activity in defective structures. Notably, the molecular states (O(p), N(p)) maintained distinct features across all models, indicating partial preservation of molecular character upon adsorption (*i.e.* weakly interacting with graphene).

Finally, the PDOS of the defect-forming C atoms in MG7 and MG8 was examined (Fig. S11). The analysis showed that localized p-orbitals from the atoms forming the non-hexagonal rings dominated the states around the Fermi level. This effect was particularly strong in MG8, where the 5- and 8-membered rings create sharp defect states directly at 0 eV. This localization explains the enhanced electronic activity and adsorption reactivity observed in the defective models compared to pristine graphene.

Conclusions

This study has shown that introducing defects significantly alters the electronic properties of graphene, transitioning it towards the metallic character. This is evidenced by increased band crossings at the Fermi level and a higher density of states near the Fermi level. These effects were most pronounced in the MG8 model, which exhibited asymmetrical bonding patterns, localized electron density, and a shift in the centre of mass of the density of states (DOS) to lower energies. Defects such as 5–7-membered rings in MG7 and 5–8-membered rings in MG8 disrupted the π-electron system, causing variations in bond lengths and bond orders that profoundly influenced graphene's electronic behaviour.

The presence of defects also strongly affected the interaction with adsorbates. CO_2 molecules adopted a parallel orientation, while NH_3 molecules tilted towards the graphene surface, optimizing interactions with defect sites. Enhanced adsorption energies were observed, particularly for MG8, with values of -15.85 kJ mol^{-1} for CO_2 and -14.78 kJ mol^{-1} for NH_3. The stronger interactions for NH_3 were attributed to accumulated electron density around defect sites and enhanced electrostatic interactions.

These findings underscore the potential of defect engineering to tailor graphene's electronic and adsorption properties for advanced gas sensing and storage applications. The observed shifts in Fermi energy and bandgap upon molecular adsorption and the enhanced density of states near the Fermi level highlight defective graphene as a promising material for selective gas sensing with improved sensitivity and specificity. This comparative study was conducted at 0 K, and further complementary finite-temperature simulations represent an important avenue for future work.

Author contributions

Daniel Moreno-Rodríguez: conceptualization, data curation, formal analysis, investigation, methodology, visualization, writing – original draft, visualization. Eva Scholtzová: conceptualization, validation, resources, writing – review & editing, supervision, project administration, funding acquisition. Hirotomo Nishihara: validation, writing – review & editing, supervision, project administration, funding acquisition.

Conflicts of interest

There are no conflicts to declare.

Data availability

The data supporting this article have been included as part of the supplementary information (SI). Supplementary information is available. See DOI: **https://doi.org/10.1039/d5qm00443h**.

Acknowledgements

This work was funded by the NextGenerationEU through the Recovery and Resilience Plan for Slovakia under project no. 09I03-03-V04-00009 (ES). HN acknowledges the financial support through JSPS Grant-in-Aid no. 23H0027. Research results were obtained using the computational resources provided by the national project National Competence Centre for High-Performance Computing (project code: 311070AKF2) funded by the European Regional Development Fund, EU Structural Funds Informatization of Society, Operational Program Integrated Infrastructure.

References

1 A. H. Castro Neto, F. Guinea, N. M. R. Peres, K. S. Novoselov and A. K. Geim, The electronic properties of graphene, *Rev. Mod. Phys.*, 2009, **81**, 109–162, DOI: **10.1103/RevModPhys.81.109**.

2 K. S. Novoselov, A. K. Geim, S. V. Morozov, D. Jiang, Y. Zhang, S. V. Dubonos, I. V. Grigorieva and A. A. Firsov, Electric field in atomically thin carbon films, *Science*, 2004, **306**, 666–669, DOI: **10.1126/science.1102896**.

3 Y. Wei and R. Yang, Nanomechanics of graphene, *Natl. Sci. Rev.*, 2019, **6**, 324–348, DOI: **10.1093/nsr/nwy067**.

4 A. A. Balandin, S. Ghosh, W. Bao, I. Calizo, D. Teweldebrhan, F. Miao and C. N. Lau, Superior thermal conductivity of single-layer graphene, *Nano Lett.*, 2008, **8**, 902–907, DOI: **10.1021/nl0731872**.

5 K. I. Bolotin, K. J. Sikes, Z. Jiang, M. Klima, G. Fudenberg, J. Hone, P. Kim and H. L. Stormer, Ultrahigh electron mobility in suspended graphene, *Solid State Commun.*, 2008, **146**, 351–355, DOI: **10.1016/j.ssc.2008.02.024**.

6 C. Lee, X. Wei, J. W. Kysar and J. Hone, Measurement of the elastic properties and intrinsic strength of monolayer graphene, *Science*, 2008, **321**, 385–388, DOI: **10.1126/science.1157996**.

7 V. Dhinakaran, M. Lavanya, K. Vigneswari, M. Ravichandran and M. D. Vijayakumar, Review on exploration of graphene in diverse applications and its future horizon, *Mater Today Proc*, Elsevier Ltd, 2020, pp. 824–828, DOI: **10.1016/j.matpr.2019.12.369**.

8 M. Zeng, Y. Liu, F. Zhao, K. Nie, N. Han, X. Wang, W. Huang, X. Song, J. Zhong and Y. Li, Metallic Cobalt Nanoparticles Encapsulated in Nitrogen-Enriched Graphene Shells: Its Bifunctional Electrocatalysis and Application in Zinc-Air Batteries, *Adv. Funct. Mater.*, 2016, **26**, 4397–4404, DOI: **10.1002/adfm.201600636**.

9 W. Lv, Z. Li, Y. Deng, Q. H. Yang and F. Kang, Graphene-based materials for electrochemical energy storage devices: Opportunities and challenges, *Energy Storage Mater.*, 2016, **2**, 107–138, DOI: **10.1016/j.ensm.2015.10.002**.

10 Y. Xu, M. G. Schwab, A. J. Strudwick, I. Hennig, X. Feng, Z. Wu and K. Müllen, Screen-Printable Thin Film Supercapacitor Device Utilizing Graphene/Polyaniline Inks, *Adv. Energy Mater.*, 2013, **3**, 1035–1040, DOI: **10.1002/aenm.201300184**.

11 T. Xie, L. Zhang, Y. Wang, Y. Wang and X. Wang, Graphene-based supercapacitors as flexible wearable sensor for monitoring pulse-beat, *Ceram. Int.*, 2019, **45**, 2516–2520, DOI: **10.1016/j.ceramint.2018.10.181**.

12 H. Kim, K. Y. Park, J. Hong and K. Kang, All-graphene-battery: Bridging the gap between supercapacitors and lithium ion batteries, *Sci. Rep.*, 2014, **4**, 1–8, DOI: **10.1038/srep05278**.

13 Y. Wang, L. Wang, T. Yang, X. Li, X. Zang, M. Zhu, K. Wang, D. Wu and H. Zhu, Wearable and Highly Sensitive Graphene Strain Sensors for Human Motion Monitoring, *Adv. Funct. Mater.*, 2014, **24**, 4666–4670, DOI: **10.1002/adfm.201400379**.

14 M. Kang, J. Kim, B. Jang, Y. Chae, J. H. Kim and J. H. Ahn, Graphene-Based Three-Dimensional Capacitive Touch Sensor for Wearable Electronics, *ACS Nano*, 2017, **11**, 7950–7957, DOI: **10.1021/acsnano.7b02474**.

15 J. Ren, C. Wang, X. Zhang, T. Carey, K. Chen, Y. Yin and F. Torrisi, Environmentally-friendly conductive cotton fabric as flexible strain sensor based on hot press reduced graphene oxide, *Carbon*, 2017, **111**, 622–630, DOI: **10.1016/j.carbon.2016.10.045**.

16 F. Xia, T. Mueller, Y. M. Lin, A. Valdes-Garcia and P. Avouris, Ultrafast graphene photodetector, *Nat. Nanotechnol.*, 2009, **4**, 839–843, DOI: **10.1038/nnano.2009.292**.

17 T. Mueller, F. Xia and P. Avouris, Graphene photodetectors for high-speed optical communications, *Nat. Photonics*, 2010, **4**, 297–301, DOI: **10.1038/nphoton.2010.40**.

18 X. Gan, R. J. Shiue, Y. Gao, I. Meric, T. F. Heinz, K. Shepard, J. Hone, S. Assefa and D. Englund, Chip-integrated ultrafast graphene photodetector with high responsivity, *Nat. Photonics*, 2013, **7**, 883–887, DOI: **10.1038/nphoton.2013.253**.

19 S. Stankovich, D. A. Dikin, G. H. B. Dommett, K. M. Kohlhaas, E. J. Zimney, E. A. Stach, R. D. Piner, S. B. T. Nguyen and R. S. Ruoff, Graphene-based composite materials, *Nature*, 2006, **442**, 282–286, DOI: **10.1038/nature04969**.

20 B. E. Yamamoto, A. Z. Trimble, B. Minei and M. N. Ghasemi Nejhad, Development of multifunctional nanocomposites with 3-D printing additive manufacturing and low graphene loading, *J. Thermoplast. Compos. Mater.*, 2019, **32**, 383–408, DOI: **10.1177/0892705718759390**.

21 D. Ward, A. Gupta, S. Saraf, C. Zhang, T. S. Sakthivel, S. Barkam, A. Agarwal and S. Seal, Functional NiAl-graphene oxide composite as a model coating for aerospace component repair, *Carbon*, 2016, **105**, 529–543, DOI: **10.1016/j.carbon.2016.04.025**.

22 P. Sun, K. Wang and H. Zhu, Recent Developments in Graphene-Based Membranes: Structure, Mass-Transport Mechanism and Potential Applications, *Adv. Mater.*, 2016, **28**, 2287–2310, DOI: **10.1002/adma.201502595**.

23 S. Goenka, V. Sant and S. Sant, Graphene-based nanomaterials for drug delivery and tissue engineering, *J. Controlled Release*, 2014, **173**, 75–88, DOI: **10.1016/j.jconrel.2013.10.017**.

24 R. Gonzalez-Rodriguez, E. Campbell and A. Naumov, Multifunctional graphene oxide/iron oxide nanoparticles for

magnetic targeted drug delivery dual magnetic resonance/fluorescence imaging and cancer sensing, *PLoS One*, 2019, **14**, e0217072, DOI: 10.1371/journal.pone.0217072.

25 S. R. Shin, Y. C. Li, H. L. Jang, P. Khoshakhlagh, M. Akbari, A. Nasajpour, Y. S. Zhang, A. Tamayol and A. Khademhosseini, Graphene-based materials for tissue engineering, *Adv. Drug Delivery Rev.*, 2016, **105**, 255–274, DOI: 10.1016/j.addr.2016.03.007.

26 K. Kostarelos and K. S. Novoselov, Graphene devices for life, *Nat. Nanotechnol.*, 2014, **9**, 744–745, DOI: 10.1038/nnano.2014.224.

27 K. Kim, Z. Lee, W. Regan, C. Kisielowski, M. F. Crommie and A. Zettl, Grain boundary mapping in polycrystalline graphene, *ACS Nano*, 2011, **5**, 2142–2146, DOI: 10.1021/nn1033423.

28 Z. Xiong, L. Zhong, H. Wang and X. Li, Structural defects, mechanical behaviors and properties of two-dimensional materials, *Materials*, 2021, **14**, 1–43, DOI: 10.3390/ma14051192.

29 J. Lahiri, Y. Lin, P. Bozkurt, I. I. Oleynik and M. Batzill, An extended defect in graphene as a metallic wire, *Nat. Nanotechnol.*, 2010, **5**, 326–329, DOI: 10.1038/nnano.2010.53.

30 W. Tian, W. Li, W. Yu and X. Liu, A review on lattice defects in graphene: Types generation effects and regulation, *Micromachines*, 2017, **8**, 163, DOI: 10.3390/mi8050163.

31 M. C. Wang, C. Yan, L. Ma, N. Hu and M. W. Chen, Effect of defects on fracture strength of graphene sheets, *Comput. Mater. Sci.*, 2012, **54**, 236–239, DOI: 10.1016/j.commatsci.2011.10.032.

32 F. Hao, D. Fang and Z. Xu, Mechanical and thermal transport properties of graphene with defects, *Appl. Phys. Lett.*, 2011, **99**, 041901, DOI: 10.1063/1.3615290.

33 G. López-Polín, C. Gómez-Navarro, V. Parente, F. Guinea, M. I. Katsnelson, F. Pérez-Murano and J. Gómez-Herrero, Increasing the elastic modulus of graphene by controlled defect creation, *Nat. Phys.*, 2015, **11**, 26–31, DOI: 10.1038/nphys3183.

34 A. Zandiatashbar, G. H. Lee, S. J. An, S. Lee, N. Mathew, M. Terrones, T. Hayashi, C. R. Picu, J. Hone and N. Koratkar, Effect of defects on the intrinsic strength and stiffness of graphene, *Nat. Commun.*, 2014, **5**, 1–9, DOI: 10.1038/ncomms4186.

35 X. Qi, X. Guo and C. Zheng, Density functional study the interaction of oxygen molecule with defect sites of graphene, *Appl. Surf. Sci.*, 2012, **259**, 195–200, DOI: 10.1016/j.apsusc.2012.07.018.

36 J. Ma, D. Alfè, A. Michaelides and E. Wang, Stone-Wales defects in graphene and other planar sp^2-bonded materials, *Phys. Rev. B: Condens. Matter Mater. Phys.*, 2009, **80**, 033407, DOI: 10.1103/PhysRevB.80.033407.

37 E. Zaminpayma, M. E. Razavi and P. Nayebi, Electronic properties of graphene with single vacancy and Stone-Wales defects, *Appl. Surf. Sci.*, 2017, **414**, 101–106, DOI: 10.1016/j.apsusc.2017.04.065.

38 M. T. Lusk and L. D. Carr, Nanoengineering defect structures on graphene, *Phys. Rev. Lett.*, 2008, **100**, 175503, DOI: 10.1103/PhysRevLett.100.175503.

39 Y. Kim, J. Ihm, E. Yoon and G. Do Lee, Dynamics and stability of divacancy defects in graphene, *Phys. Rev. B: Condens. Matter Mater. Phys.*, 2011, **84**, 075445, DOI: 10.1103/PhysRevB.84.075445.

40 A. V. Krasheninnikov, P. O. Lehtinen, A. S. Foster and R. M. Nieminen, Bending the rules: Contrasting vacancy energetics and migration in graphite and carbon nanotubes, *Chem. Phys. Lett.*, 2006, **418**, 132–136, DOI: 10.1016/j.cplett.2005.10.106.

41 G. Do Lee, C. Z. Wang, E. Yoon, N. M. Hwang, D. Y. Kim and K. M. Ho, Diffusion, coalescence, and reconstruction of vacancy defects in graphene layers, *Phys. Rev. Lett.*, 2005, **95**, 205501, DOI: 10.1103/PhysRevLett.95.205501.

42 J. C. Meyer, C. Kisielowski, R. Erni, M. D. Rossell, M. F. Crommie and A. Zettl, Direct imaging of lattice atoms and topological defects in graphene membranes, *Nano Lett.*, 2008, **8**, 3582–3586, DOI: 10.1021/nl801386m.

43 J. Kotakoski, J. C. Meyer, S. Kurasch, D. Santos-Cottin, U. Kaiser and A. V. Krasheninnikov, Stone-Wales-type transformations in carbon nanostructures driven by electron irradiation, *Phys. Rev. B: Condens. Matter Mater. Phys.*, 2011, **83**, 245420, DOI: 10.1103/PhysRevB.83.245420.

44 A. El-Barbary, H. Telling, P. Ewels, I. Heggie and R. Briddon, Structure and energetics of the vacancy in graphite, *Phys. Rev. B: Condens. Matter Mater. Phys.*, 2003, **68**, 144107, DOI: 10.1103/PhysRevB.68.144107.

45 A. E. Romanov, M. A. Rozhkov and A. L. Kolesnikova, Disclinations in polycrystalline graphene and pseudographenes. Review, *Lett. Mater.*, 2018, **8**, 384–400.

46 O. V. Yazyev and S. G. Louie, Topological defects in graphene: Dislocations and grain boundaries, *Phys. Rev. B: Condens. Matter Mater. Phys.*, 2010, **81**, 195420, DOI: 10.1103/PhysRevB.81.195420.

47 D. A. F. Martins, K. A. Lima, F. F. Monteiro, M. L. Pereira, L. A. Ribeiro and A. Macedo-Filho, Examining O_2 adsorption on pristine and defective popgraphene sheets: A DFT study, *J. Mol. Model.*, 2023, **29**, 1–9, DOI: 10.1007/S00894-023-05692-4.

48 X. Qi, X. Guo and C. Zheng, Density functional study the interaction of oxygen molecule with defect sites of graphene, *Appl. Surf. Sci.*, 2012, **259**, 195–200, DOI: 10.1016/j.apsusc.2012.07.018.

49 Q. Zhou, L. Yuan, X. Yang, Z. Fu, Y. Tang, C. Wang and H. Zhang, DFT study of formaldehyde adsorption on vacancy defected graphene doped with B, N, and S, *Chem. Phys.*, 2014, **440**, 80–86, DOI: 10.1016/J.CHEMPHYS.2014.06.016.

50 G. R. Yazdi, F. Akhtar, I. G. Ivanov, S. Schmidt, I. Shtepliuk, A. Zakharov, T. Iakimov and R. Yakimova, Effect of epitaxial graphene morphology on adsorption of ambient species, *Appl. Surf. Sci.*, 2019, **486**, 239–248, DOI: 10.1016/j.apsusc.2019.04.247.

51 M. R. Fiorentin, R. Gaspari, M. Quaglio, G. Massaglia and G. Saracco, Nitrogen doping and CO_2 adsorption on graphene: A thermodynamical study, *Phys Rev B*, 2018, **97**, 155428, DOI: 10.1103/PhysRevB.97.155428.

52 A. Sahithi and K. Sumithra, Adsorption and sensing of CO and NH_3 on chemically modified graphene surfaces, *RSC Adv.*, 2020, **10**, 42628–42634, DOI: **10.1039/d0ra06760a**.

53 N. Tit, K. Said, N. M. Mahmoud, S. Kouser and Z. H. Yamani, Ab-initio investigation of adsorption of CO and CO_2 molecules on graphene: Role of intrinsic defects on gas sensing, *Appl. Surf. Sci.*, 2017, **394**, 219–230, DOI: **10.1016/j.apsusc.2016.10.052**.

54 H. Nishihara, T. Simura, S. Kobayashi, K. Nomura, R. Berenguer, M. Ito, M. Uchimura, H. Iden, K. Arihara, A. Ohma, Y. Hayasaka and T. Kyotani, Oxidation-Resistant and Elastic Mesoporous Carbon with Single-Layer Graphene Walls, *Adv. Funct. Mater.*, 2016, **26**, 6418–6427, DOI: **10.1002/ADFM.201602459**.

55 W. Yu, T. Yoshii, A. Aziz, R. Tang, Z. Z. Pan, K. Inoue, M. Kotani, H. Tanaka, E. Scholtzová, D. Tunega, Y. Nishina, K. Nishioka, S. Nakanishi, Y. Zhou, O. Terasaki and H. Nishihara, Edge-Site-Free and Topological-Defect-Rich Carbon Cathode for High-Performance Lithium-Oxygen Batteries, *Adv. Sci.*, 2023, **10**, 2300268, DOI: **10.1002/ADVS.202300268**.

56 A. Ohma, Y. Furuya, T. Mashio, M. Ito, K. Nomura, T. Nagao, H. Nishihara, H. Jinnai and T. Kyotani, Elucidation of oxygen reduction reaction and nanostructure of platinum-loaded graphene mesosponge for polymer electrolyte fuel cell electrocatalyst, *Electrochim. Acta*, 2021, **370**, 137705, DOI: **10.1016/J.ELECTACTA.2020.137705**.

57 Z. Shen, W. Yu, A. Aziz, K. Chida, T. Yoshii and H. Nishihara, Sequential Catalysis of Defected-Carbon and Solid Catalyst in Li-O_2 Batteries, *J. Phys. Chem. C*, 2023, **127**, 6239–6247, DOI: **10.1021/ACS.JPCC.3C01042/ASSET/IMAGES/MEDIUM/JP3C01042_0005.GIF**.

58 W. Yu, Z. Shen, T. Yoshii, S. Iwamura, M. Ono, S. Matsuda, M. Aoki, T. Kondo, S. R. Mukai, S. Nakanishi and H. Nishihara, Hierarchically Porous and Minimally Stacked Graphene Cathodes for High-Performance Lithium–Oxygen Batteries, *Adv. Energy Mater.*, 2024, **14**, 2303055, DOI: **10.1002/AENM.202303055**.

59 G. Kresse and J. Hafner, Ab-initio molecular-dynamics for open-shell transition-metals, *Phys Rev B: Condens. Matter Mater. Phys.*, 1993, **48**, 13115–13118, DOI: **10.1103/PhysRevB.48.13115**.

60 G. Kresse and J. Furthmuller, Efficiency of ab-initio total energy calculations for metals and semiconductors using a plane-wave basis set, *Comput. Mater. Sci.*, 1996, **6**, 15–50, DOI: **10.1016/0927-0256(96)00008-0**.

61 J. P. Perdew, K. Burke and M. Ernzerhof, Generalized gradient approximation made simple, *Phys. Rev. Lett.*, 1996, **77**, 3865–3868, DOI: **10.1103/PhysRevLett.77.3865**.

62 S. Grimme, J. Antony, S. Ehrlich and H. Krieg, A consistent and accurate ab initio parametrization of density functional dispersion correction (DFT-D) for the 94 elements H-Pu, *J. Chem. Phys.*, 2010, **132**, 154104, DOI: **10.1063/1.3382344**.

63 T. A. Manz and N. G. Limas, Introducing DDEC6 atomic population analysis: Part 1. Charge partitioning theory and methodology, *RSC Adv.*, 2016, **6**, 47771–47801, DOI: **10.1039/c6ra04656h**.

64 N. G. Limas and T. A. Manz, Introducing DDEC6 atomic population analysis: Part 2. Computed results for a wide range of periodic and nonperiodic materials, *RSC Adv.*, 2016, **6**, 45727–45747, DOI: **10.1039/c6ra05507a**.

65 B. Silvi and A. Savin, Classification of chemical bonds based on topological analysis of electron localization functions, *Nature*, 1994, **371**, 683–686, DOI: **10.1038/371683a0**.

66 S. Shaik, D. Danovich, W. Wu and P. C. Hiberty, Charge-shift bonding and its manifestations in chemistry, *Nat. Chem.*, 2009, **1**, 443–449, DOI: **10.1038/nchem.327**.